Continental Shelf Research 30 (2010) 633–642

Contents lists available at ScienceDirect

Continental Shelf Research

journal homepage: www.elsevier.com/locate/csr

Tsunami–tide interactions: A Cook Inlet case study

Zygmunt Kowalik [a,*], Andrey Proshutinsky [b]

[a] Institute of Marine Science, University of Alaska, Fairbanks, Alaska, AK 99775, USA
[b] Woods Hole Oceanographic Institution, Woods Hole, MA 02543, USA

ARTICLE INFO

Article history:
Received 17 December 2008
Received in revised form
22 September 2009
Accepted 1 October 2009
Available online 9 October 2009

Topical issue on "Tides in Marginal Seas" (in memory of Professor Alexei V. Nekrasov). The issue is published with support of the North Pacific Marine Science Organization (PICES).

Keywords:
Tide and tsunami
Nonlinear interactions
Cook Inlet
Numerical modeling

ABSTRACT

First, we investigated some aspects of tsunami–tide interactions based on idealized numerical experiments. Theoretically, by changing total ocean depth, tidal elevations influence the speed and magnitude of tsunami waves in shallow regions with dominating tidal signals. We tested this assumption by employing a simple 1-D model that describes propagation of tidal waves in a channel with gradually increasing depth and the interaction of the tidal waves with tsunamis generated at the channel's open boundary. Important conclusions from these studies are that computed elevations by simulating the tsunami and the tide together differ significantly from linear superposing of the sea surface heights obtained when simulating the tide and the tsunami separately, and that maximum tsunami–tide interaction depends on tidal amplitude and phase. The major cause of this tsunami–tide interaction is tidally induced ocean depth that changes the conditions of tsunami propagation, amplification, and dissipation. Interactions occur by means of momentum advection, bottom friction, and variable water flux due to changing total depth and velocity. We found the major cause of tsunami–tide interactions to be changing depth. Secondly, we investigate tsunami–tide interactions in Cook Inlet, Alaska, employing a high-resolution 2-D numerical model. Cook Inlet has high tides and a history of strong tsunamis and is a potential candidate for tsunami impacts in the future. In agreement with previous findings, we find that the impacts of tsunamis depend on basin bathymetries and coastline configurations, and they can, in particular, depend on tsunami–tide interactions. In regions with strong tides and tsunamis, these interactions can result in either intensification or damping of cumulative tsunami and tide impacts, depending on mean basin depth, which is regulated by tides. Thus, it is not possible to predict the effect of tsunami–tide interaction in regions with strong tides without making preliminary investigations of the area. One approach to reduce uncertainties in tsunami impact in regions with high tides is to simulate tsunamis together with tidal forcing.

1. Introduction

As a tsunami propagates in the ocean as a short-term event, it interacts with various processes and can be influenced or modified by these interactions (e.g. Dixon and Tawn, 1997; Weisz and Winter, 2005; Kowalik et al., 2006). However, in the real world, most of these interactions can be disregarded when predicting tsunamis because water motions associated with tsunamis are much stronger than other "background" motions; for example, the effect of tsunami–tide interaction can be estimated as a linear superposition of sea level change due to both tide and tsunami surges (see The Sea, Tsunamis, 2009). On the other hand, for some regions with very strong tides, the nonlinear effects may be important and should be evaluated (Kowalik et al., 2006). Because the near-shore bathymetry is important for the run-up computation, Weisz and Winter (2005) demonstrated that depth changes caused by tides should not be neglected in the run-up. In addition, Kowalik et al. (2006) hypothesized that a significant effect of tsunami–tide interaction should be observed in the tidal and tsunami currents.

Here, we focus on tsunami–tide interactions that affect the US West Coast, including Alaska, where tidal magnitudes are high and tsunami events are relatively frequent. These conditions were recognized by Houston and Garcia (1978), who used predicted tides to calculate tsunami run-up heights for tsunami flood insurance maps; and by Mofjeld et al. (2007) for evaluation of probability distribution of maximum tsunami amplitudes and tides. Mofjeld et al. (1997) also showed that the significant effect of the large tides and the sea level elevation on tsunami run-up and flooding has to be taken into account when historical and paleotsunamis are computed and compared against tsunami deposits.

Investigating tsunami–tide interactions we first describe a high-resolution model (Section 2) and then employ this model to study idealized scenarios of tsunami–tide interaction (Section 3).

* Corresponding author.
E-mail address: ffzk@ims.uaf.edu (Z. Kowalik).

0278-4343/$ - see front matter © 2009 Elsevier Ltd. All rights reserved.
doi:10.1016/j.csr.2009.10.004

In Section 4 we discuss results of tsunami–tide interactions in Cook Inlet, which has very strong tides and is a potential candidate for future tsunami impacts (Lander and Lockridge, 1989). Section 5 provides a summary of our findings and offers recommendations.

2. Model description

Here, we analyze several examples of linear and nonlinear tsunami and tide interactions, based mainly on Kowalik et al. (2006). The "shallow water" Eqs. (1)–(3) are employed to simulate tides and tsunamis

$$\frac{\partial u}{\partial t}+u\frac{\partial u}{\partial x}+v\frac{\partial u}{\partial y}-fv=-g\frac{\partial \zeta}{\partial x}-\frac{1}{\rho D}\tau_x^b, \quad (1)$$

$$\frac{\partial v}{\partial t}+u\frac{\partial v}{\partial x}+v\frac{\partial v}{\partial y}+fu=-g\frac{\partial \zeta}{\partial y}-\frac{1}{\rho D}\tau_y^b, \quad (2)$$

$$\frac{\partial \zeta}{\partial t}+\frac{\partial uD}{\partial x}+\frac{\partial vD}{\partial y}=0, \quad (3)$$

where x and y are the coordinate axes, u and v the vertically mean (averaged) velocities along the x and y coordinates, respectively, t is time, f the Coriolis parameter ($f=2\Omega\sin\phi$) and a function of Earth's angular velocity ($\Omega=7.29\times10^{-5}\,s^{-1}$) and latitude ($\phi$), ρ denotes seawater density, ζ is the sea level change relative to mean sea level, $D=H+\zeta$ the total depth, where H is the mean depth, and τ_x^b and τ_y^b are components of the bottom friction proportional to the square of the velocity, ($\tau_x^b=\rho ru\sqrt{u^2+v^2}$ and $\tau_y^b=\rho rv\sqrt{u^2+v^2}$). The dimensionless friction coefficient r is defined as $r=2.6\times10^{-3}$. The components of the water flux vector uD and vD in the equation of continuity denote vertically integrated horizontal water transport extended from the free surface to the bottom.

Initially, the dependent variables in the integration domain of the model Eqs. (1)–(3) are defined as zero. Along the solid boundaries, we assume the normal to the boundary velocity component to be zero. The tidal and tsunami signals are prescribed at open boundaries via sea level disturbances, and we proceed as follows: first, the tides are calculated for approximately 20 tidal periods, and then a tsunami is generated and its propagation is recorded/investigated until it reaches the point of interest. After tsunami generation, two kinds of radiation conditions are applied. The first radiation condition is based on known tidal amplitude and current as defined by Flather (1976). The second radiation condition is constructed from a combination of the sinusoidal (tidal) signal and the wave radiating toward the open boundary (tsunami), according to Durran (1999).

To solve Eqs. (1)–(3) with initial and boundary conditions, a semi-implicit finite-difference scheme with central differences on an Arakawa C grid is employed, following Kowalik et al. (2005). Also see details of tsunami models and algorithms at http://www.sfos.uaf.edu/directory/faculty/kowalik/).

3. Tsunami–tide interaction in an idealized channel

One of the expected effects of tsunami–tide interactions is associated with changing full water depth due to tides. At different tide stages, the tsunami propagates in "shallow" or "deep" water, and the tsunami's arrival time is shorter at high tide (deep water) than at low tide because tsunami propagation speed ($c=\sqrt{g(H+\zeta)}$) depends on total water depth. If the total depth is less than the mean water depth, the tsunami propagation speed is reduced and, consequently, the tsunami arrival time increases, and vice versa. Another effect is reflected in total sea level change (tide plus tsunami). At low tide, when sea level may be a few meters less than the undisturbed depth, the tsunami-related sea level rise may have no damaging effect if linear superposition of tsunami and tide is considered. However, the question is whether the linear superposition assumption is sufficient to describe tide–tsunami interactions in shallow water. To answer this question, we investigated how tsunamis and tides interact based on analyses of terms in equations of motion and continuity. Interactions occur by means of momentum advection, bottom friction, and variable water flux due to changing total depth and velocity.

In a simple approach, we used Eqs. (1)–(3) to study tsunami–tide interactions in a one-dimensional, 1000-km-long channel with depths gradually decreasing from 1000 m at its left side to 20 m at its right side (Fig. 1). At the left side, we assumed an open boundary where tidal elevations and tsunamis were generated, and at the right side, we prescribed a wall with $u=0$. No run-up was considered in order to simplify this problem and to investigate how tides and tsunamis interact at a wall.

First, we simulated tidal motion by prescribing characteristics of a semi-diurnal M_2 tide with an amplitude of 100 cm. When a periodic stationary state solution was reached, we continued calculations of tides and added tsunamis. Sixty step-shaped tsunamis 100 cm high with 12.42 min duration (Fig. 1) were

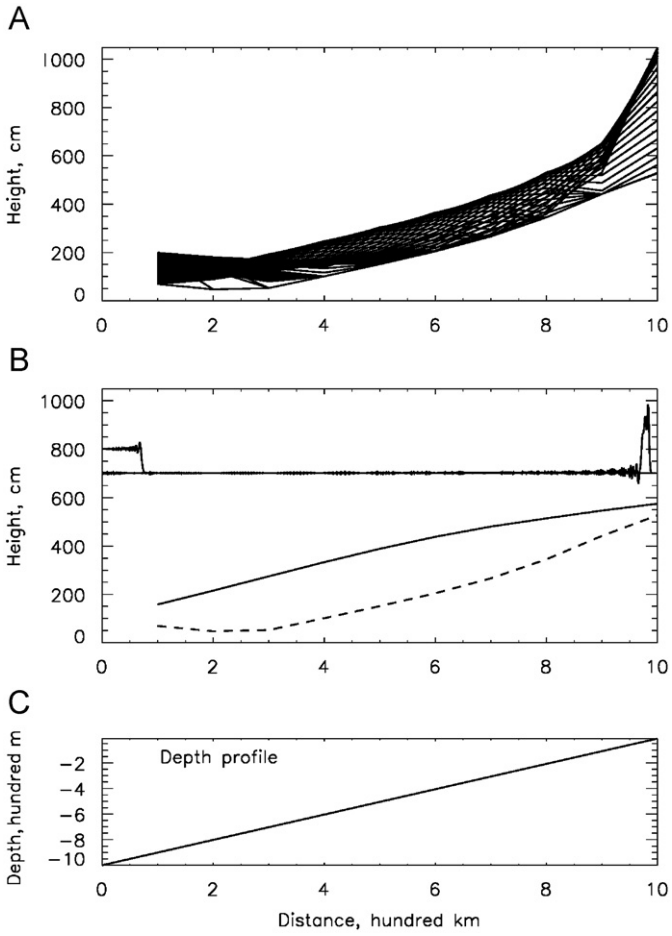

Fig. 1. Maximums of sea surface height (SSH) along a 1000-km-long channel at different tidal phases. Panel (A) shows SSH maximums due to tsunamis and tides combined. There are 60 lines showing interactions for 60 tsunamis generated at the left open boundary during different tidal phases, with time intervals of 12.42 min. Panel (B) shows tsunami (continuous line) and tide (dashed line) maximums simulated separately. Panel (C) shows a 1000-km-long channel with depth gradually changing from 1000 m at its left side to approximately 20 m at its right side. Note that the tsunami signal wave forms are shown as an example at the left and write channel walls and are offset from "0" level by 700 cm.

generated at the left side of the channel at different tidal phases. This approach allowed us to analyze tsunami–tide interaction during M2 tidal cycle (12.42 h) with interval of 12.42 min. After each tsunami generation, we continued joint tsunami and tide calculations until the tsunami reached the right wall of this channel and maximum sea level was observed. Then the next tsunami was generated, and etc. These simulations allowed us to investigate how tsunami magnitude depends on tidal phase. Fig. 1 summarizes the results of this "standard" experiment and shows a range of tsunami and tide changes along the channel as well as results of their superposition and interaction. Tide and tsunami magnitudes increased in the shallow water region, and maximums were reached at the right wall. Some nonlinearity is evident from differing patterns in the distribution of tidal and tsunami maximums along the channel: the rate of tidal height growth is much stronger than the rate of tsunami growth when the ocean depth decreases. We speculate that starting at a depth less than 200 m allows interactions between tidal and tsunami signals to be detected, at least in this idealized case.

Line 1 in Fig. 2 shows how tsunami height changes at the right channel wall are dependent on tidal phase. The tsunami reached its maximum 2.5 h after high tide at the right channel wall, and the tsunami minimum was observed at rising tide—several hours before high tide. We also carried out several numerical experiments to evaluate the roles of different equation terms in tsunami dynamics at different tidal phases. Results of these experiments are shown in Table 1 and Fig. 2. The first experiment, discussed above, is a "standard" case that includes all terms from Eqs. (1)–(3); it is listed as experiment #1 in Table 1 and Fig. 2. In the second experiment, we investigated the role of effects associated with the total depth, $D=H+\zeta$. In this experiment, $D=H+\zeta$ was replaced with the mean depth $D=H$, which influenced the bottom friction term because $\tau^b/\rho D$ and also because of the terms of water flux in the equation of continuity (3).

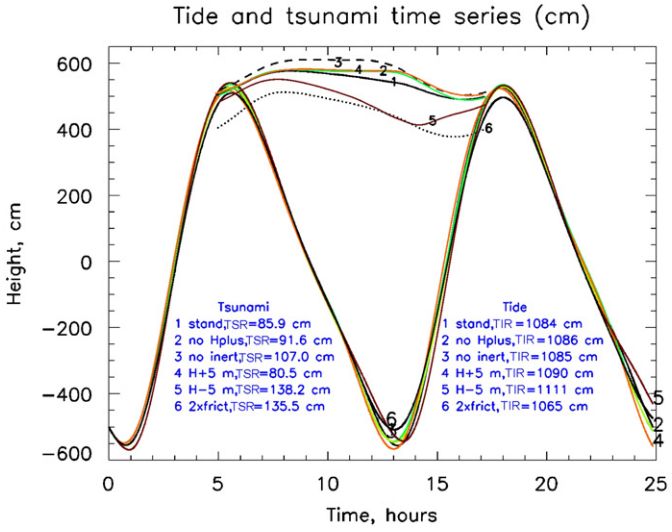

Fig. 2. Computed tide and tsunami time series at the right channel wall. Tide: sea level as a function of time. Tsunami: the maximum amplitude as related to different tidal phases. Lines 1–6 depict tsunami height maximums at the right channel wall for a set of numerical experiments described in Table 1. The TSR indicator shows a range of tsunami height changes at the right channel wall, depending on tidal phase. For tides, TIR shows a difference between high and low tide at the right channel wall.

In general, maximum tsunami distribution is similar to a standard model run, but tsunami maximum heights at low tide were higher than in experiment #1. This is because the replacement of $D=H+\zeta$ with $D=H$ results in reduction of bottom friction (in this case $D=H$ instead of $D<H$ because of low tide) and, consequently, increased tsunami height. The maximum effect of this term is expected at low tide, but it also related to water flux changes in Eq. (3), so the superposition of these two effects determines the shape of curves #1 and #2 in Fig. 2 with tsunami minimums just about 2.5 h before high tide. We also assume that this effect is responsible for increase in differences ("TSR", or "tsunami range" in Fig. 2) between maximum and minimum tsunami heights during a tidal cycle (an increase from 85.9 to 91.6 cm, Fig. 2). Tidal range ("TIR" in Fig. 2, which shows a difference between high and low tide) also increased by 2 cm (less than a 0.2% change relative to a standard model run). Fig. 3 illustrates the role of friction in tsunami–tide interactions and shows that maximum tidal friction is observed during a phase of growing sea level at the right channel wall. Bottom friction associated with tsunami and tide together is higher than tidal friction only, and it changes depending on tidal phase. The difference between bottom friction due to tide only and tsunami and tide together characterizes the effect of tsunami friction at different tidal phases, but only to some degree because of the nonlinearity of this term. Fig. 2 indicates that total bottom friction is dominated by tidal friction, but the tsunami's role increases when tidal friction is minimal (at low and high tide, see Fig. 3).

The major goal of experiment #3 was to evaluate the role of terms responsible for momentum advection in Eqs. (1) and (2). In this experiment, these terms were omitted. It is surprising that omitting momentum advection leads to an increase in tsunami height compared to the standard model run. The general shape of line #3 did not change relative to the standard model run but, at all tidal phases, the tsunami maximum was higher than in experiment #1. The dependence of tsunami height on tidal phase in this experiment also increased, and TSR reached 107 cm, which is 19.2% of the mean tsunami height, larger than in the standard model run. The momentum advection terms are responsible for the strong nonlinear effects, and their role must be more

Table 1
Numerical experiments in an idealized channel.

Experiment	Tsunami height and % of change (max–min) relative to mean		Tide height and % of change (max–min) relative to standard run	
	Max/min (cm)	Change (%)	Max/min (cm)	Change (%)
1. "standard": full model run	576/490	15.6	527/−556	0.0
2. "no $D=H+\zeta$": $D=H$	580/488	17.0	540/−540	0.2
3. "no inert": no momentum advection	611/504	19.2	528/−557	0.1
4. "$H+5$ m": $H=H+5$ m	582/502	14.7	523/−567	0.5
5. "$H-5$ m": $H=H-5$ m	551/413	31.9	541/−569	1.2
6. "2xfric": doubled bottom friction	513/377	30.3	509/−555	1.8
7. No friction, no advection, but $D=H+\zeta$	741/635	15.4	550/−600	1.0
8. No friction, no advection and $D=H$	678/678	0.0	550/−550	0.0

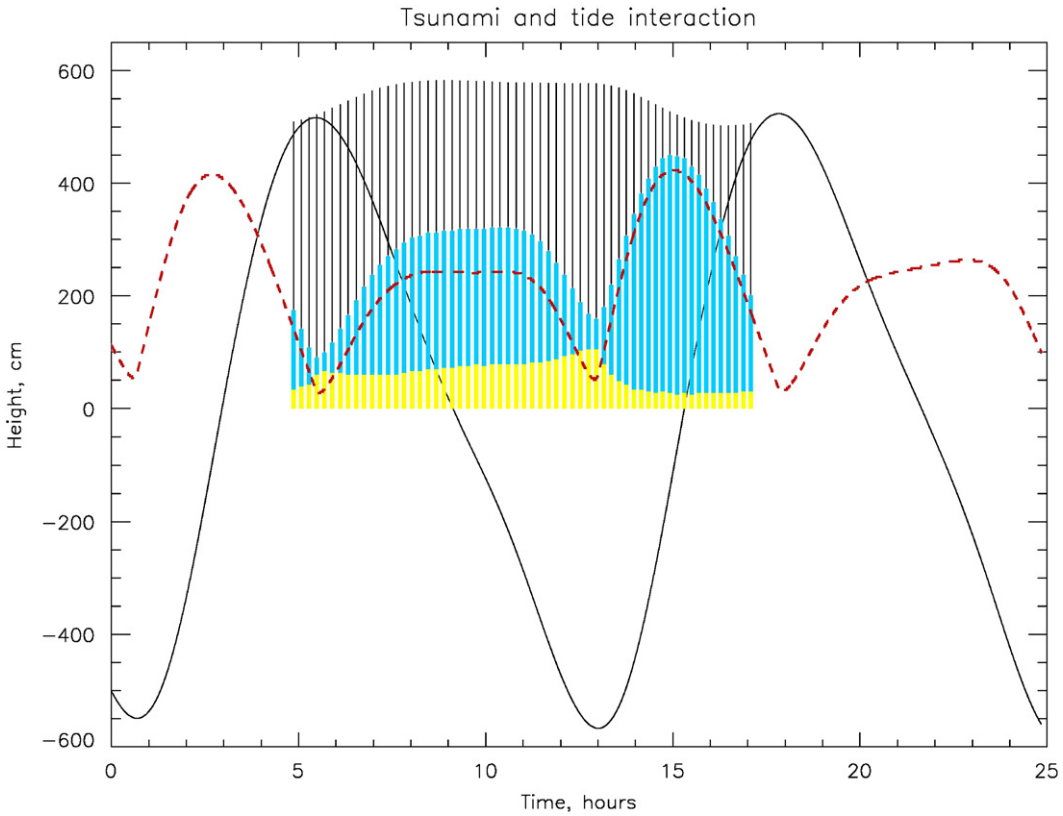

Fig. 3. Tsunami–tide interactions. Vertical black bars show tsunami heights (cm) at the right channel wall at different tidal phases. The solid black line shows a time series of tidal sea level (cm). The dashed red line depicts total bottom friction due to tide only (integrated along the channel for each moment in time). Vertical blue bars show total bottom friction due to integration of tides and tsunamis along the channel when the tsunami hits the right channel wall. Note that maximum tidal friction is observed when tidal currents are strongest and sea level is growing at the right channel wall. Yellow bars show the difference between friction calculated for tsunami and tide combined and for tide only.

pronounced during run-up processes. In these numerical experiments, the inclusion of momentum advection in the standard model run reduced tsunami heights at all tidal phases.

In experiments #4 and #5, we investigated the role of the ocean mean depth in tsunami amplification. In experiment #4, the mean depth of the channel was increased by 5 m (close to mean tide amplitude at the right channel wall), and in experiment #5, it was reduced by 5 m. Tsunami amplification in experiment #4 did not differ significantly from the standard model run. Line #4 (in Fig. 2) is practically identical to line #2, which represents tsunami amplification for the mean depth. But the results of experiment #5, when mean channel depth was reduced by 5 m, differ significantly from the results of the standard model run. Reduction of channel depth resulted in (a) an increase in tidal magnitude, (b) a reduction of tsunami maximums at all tidal phases, (c) an increase in differences between tsunami maximums and minimums (TSR=138 cm), and (d) maximum changes observed relative to the standard model run (31.9%). This tsunami behavior is caused by increase in bottom dissipation in the shallower channel as compared to tsunami propagation in the deeper channel.

In experiment #6, we doubled the bottom friction coefficient in the standard model run. This resulted in significant reduction of tsunami maximums, some reduction of tidal magnitude, and an increase in the difference between the tsunami maximum and minimum observed at different tidal phases (TSR=135.5, Fig. 2).

In experiment #7 (Table 1, Fig. 4), we repeated our calculations without friction and advection but with $D=H+\zeta$. Results of this experiment showed that bottom friction and advection are not the major causes of tsunami height changes at different tidal phases, but momentum flux plays an important role in tsunami–tide interaction. In order to fully confirm this, in experiment #8 (Table 1), we repeated our calculations without friction and advection and assumed that $D=H$. In this case, tsunami amplitude was independent of tidal phase and remained constant (678 cm, Table 1).

Based on these experiments, we can conclude that, without friction and inertial effects, the major cause of tsunami–tide interactions is changing depth (expressed in fluxes in the equation of continuity (3)) in the channel due to tides. In more real situations, with bottom friction and advection, there is interplay among all factors influencing tsunami–tide interactions, and, in general, the maximum variability in tsunami potential due to interactions with tides can be expected in the shallow regions.

In this paper, we do not investigate tsunami–tide interaction for the case of run-up where advective terms in Eqs. (1) and (2) are the important factors. These conditions are discussed by Kowalik et al. (2006).

4. Tsunami–tide interactions in Cook Inlet

The results discussed above demonstrate that employing Eqs. (1)–(3) for tsunami prediction, when both tsunamis and tides are strong and comparable in magnitude, results in tsunami–tide interactions being responsible for up to 20% of tsunami magnitude change, depending on the tidal phase at tsunami generation moment.

This potentially nonlinear character of tsunami–tide interaction must be taken into account in regions with high tides and significant tsunamis, such as Alaskan coastal waters. To investigate processes taking place during tsunami–tide interactions, we applied our models and methods to Cook Inlet (CI), where the shelf is wide and relatively shallow. The depth at the entrance to CI is

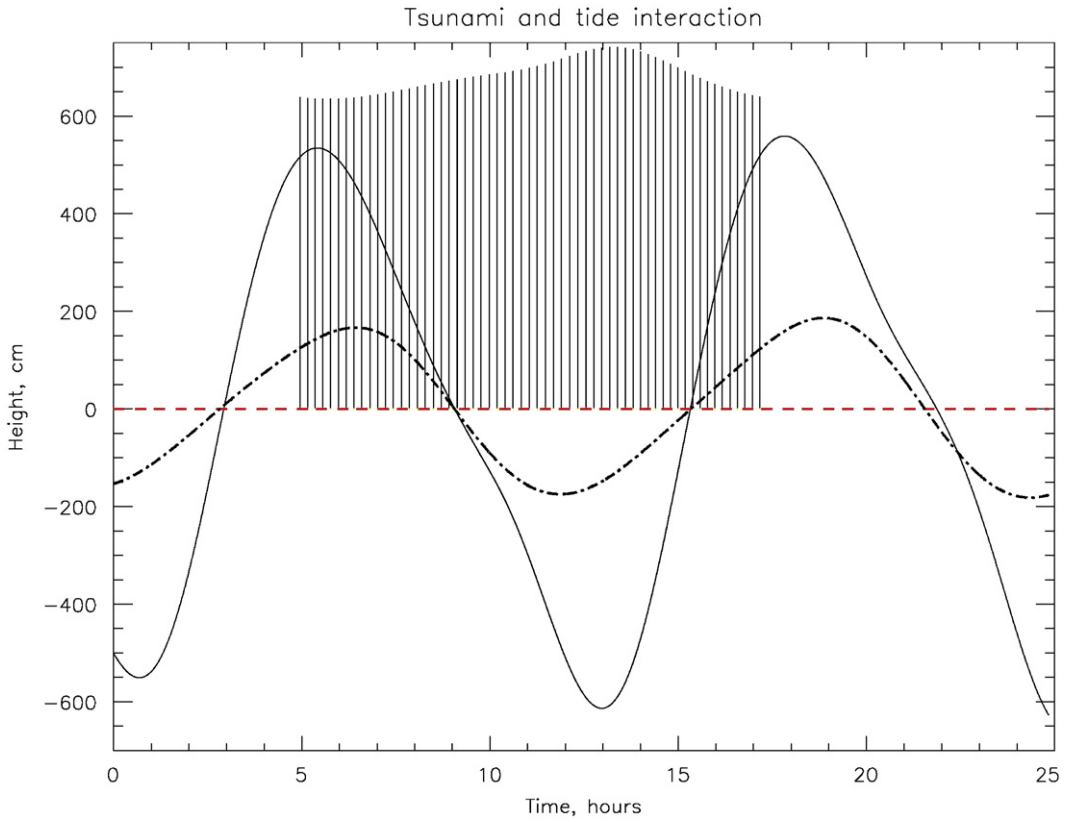

Fig. 4. Tsunami–tide interactions for a numerical experiment conducted without friction and advective terms. The solid black line shows a tidal sea level time series at the right channel wall. Vertical bars show the tsunami height maximum at the right channel wall at different tidal phases. The dashed red line depicts bottom friction and shows that bottom friction in this experiment was zero. The dotted-dashed line shows anomalies in mean channel depth integrated from the left to the right wall. The tsunami minimum is observed with increased mean channel depth, and the maximum when depth is close to minimum. There is a shift in time between depth and tsunami height extremes because the maximum tsunami height is registered at the right wall where tide–tsunami interaction reaches its maximum.

approximately 100 m, and the inlet's low land relief allows extensive inundation and very strong tides (up to 12 m). The Cook Inlet tidal dynamics have been studied both empirically and numerically. The first Cook Inlet tidal stream atlas was produced by Matthews and Mungall (1972) from the Institute of Marine Science, University of Alaska Fairbanks, based on a small set of observations and results from a 2-D low-resolution numerical model. From 1973 through 1975, NOAA has carried out a comprehensive circulation survey of Cook Inlet (Patchen et al., 1981) and these data are still in use in many numerical and application studies. For instance, the "Numerical modeling of extreme tidal conditions in upper Cook Inlet, Alaska" (1993) report by D. Raney is completely based on the NOAA information cited above. The basic numerical model utilized for this investigation is a version of a 2-D depth-averaged model developed by the US Army Corps of Engineers Waterways Experimental Station (WES) in Vicksburg, Mississippi. The model results showed that the simulated tidal range was basically correct, but the modeled tide heights were underestimated. Two other models (POM and TRIM5) with relatively high resolution (2 km) were used in 1998 to simulate tidal currents in order to model oil spill trajectories (see Cook Inlet Oceanography Workshop, 2000, Johnson and Okkonen (Eds.), 2000), but the quality of the simulations was not discussed and the authors warned users that the information about currents should not be used for navigation purposes. Recently Ezer et al. (2008), Ezer and Liu (2009), and Oey et al. (2007) have simulated tidal dynamics of CI taking into account wetting and drying conditions (tidal run-up) in order to better reproduce tidal dynamics in its influence on CI environmental conditions but tidal parameters were not discussed.

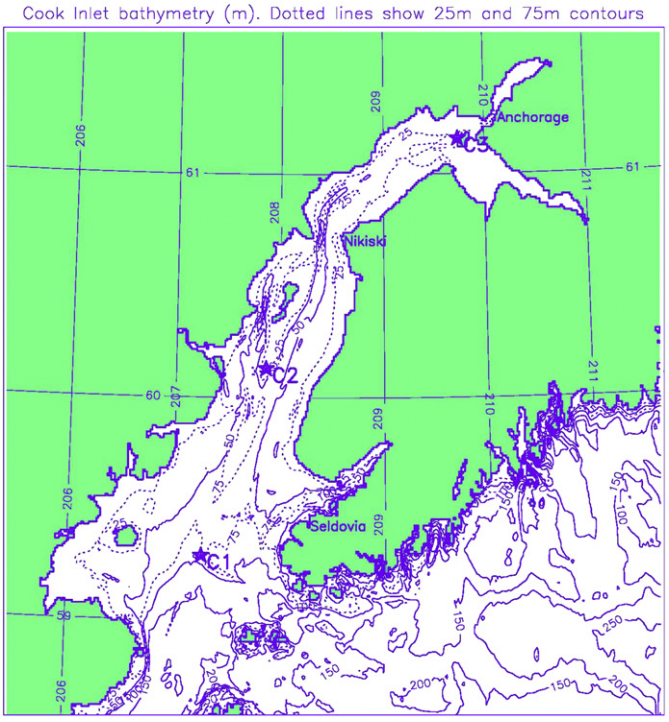

Fig. 5. Cook Inlet model domain with horizontal resolution of 1 km. Bathymetry (solid lines) is shown in meters. Dotted lines show 25 and 75 m contours.

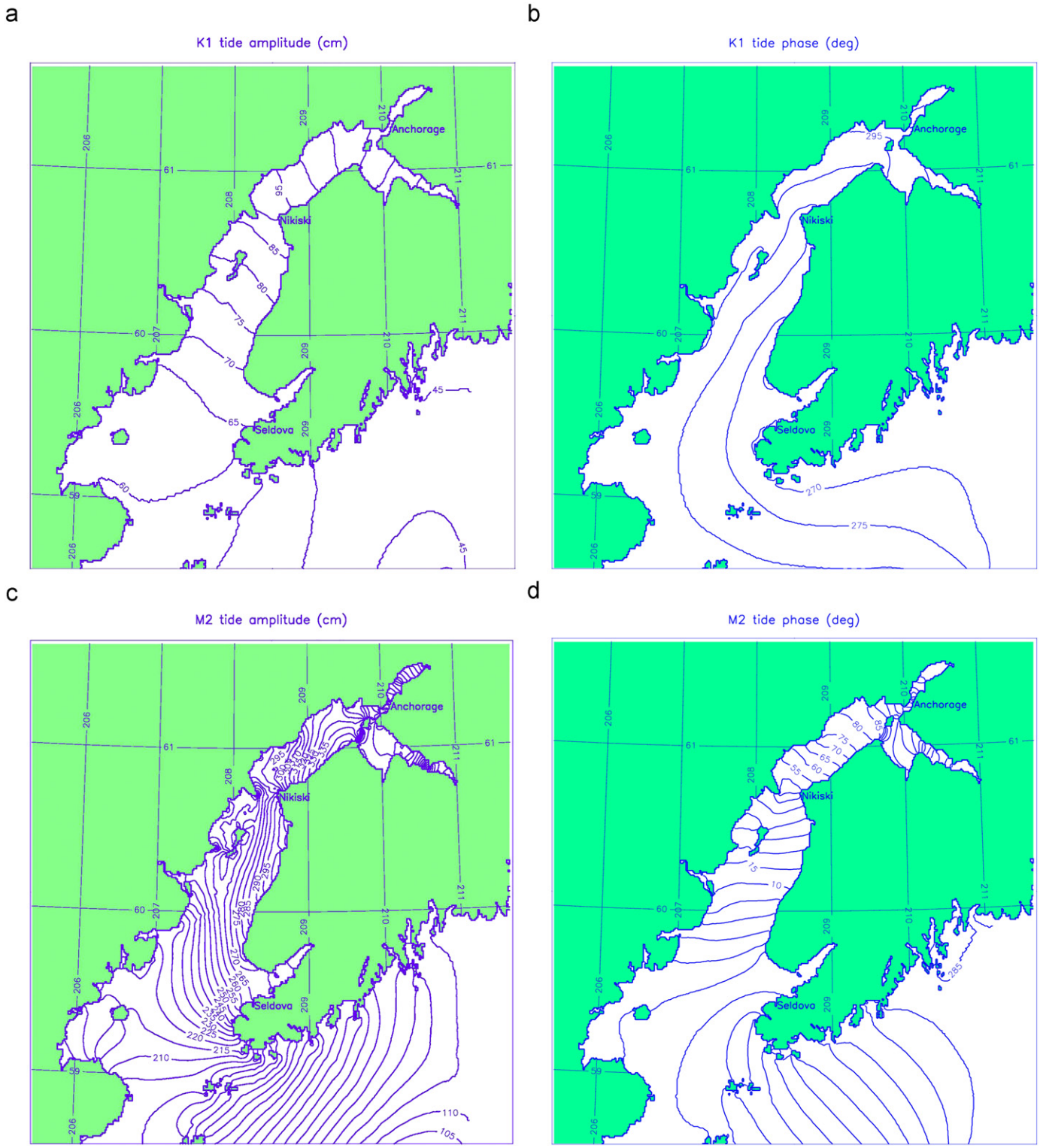

Fig. 6. Tidal charts for K1 and M2 major diurnal and semi-diurnal constituents in Cook Inlet. Amplitudes of tides are in cm and phases are in degrees.

For this study we applied model (1–3) to reproduce CI tidal dynamics and to investigate how CI tides can influence tsunamis in this region. The CI model domain (Fig. 5) has a spatial resolution of 1 km, and we simulated seven major tidal constituents (M2, S2, N2, K2, K1, O1, and Q1). Model boundary conditions were obtained from satellite-based archives of tidal constituents for the Gulf of Alaska and the North Pacific Ocean. For this purpose, we used the FES95.1/2 models, which stem from the earlier pure hydrodynamic finite element solution FES94.1 (Egbert et al., 1994).

First, each tidal constituent was simulated separately for at least 20 tidal cycles, and amplitudes and phases for sea level elevations and velocity components were estimated after reaching a dynamic stationary state when amplitudes and phases of tide stopped changing from cycle to cycle. The model results included

Table 2
Observed/simulated amplitude (Ampl.) and phase for semidiurnal constituents M2, S2, N2, and K2.

Station	M2 constituent		S2 constituent		N2 constituent		K2 constituent	
	Ampl. (cm)	Phase (deg)	Ampl. (cm)	Phase (deg)	Ampl. (cm)	Phase (deg)	Ampl. (cm)	Phase (deg)
Nikiski	251/292	030/039	087/105	062/072	049/050	359/017	025/017	054/076
Seldovia	223/265	324/339	082/088	359/007	047/042	297/304	023/019	353/349
Anchorage	353/287	108/109	100/148	150/150	060/098	082/085	027/048	142/151

Note the phases are Greenwich phase lags.

Table 3
Same as in Table 2 but for diurnal constituents.

Station	O1 constituents		K1 constituents		Q1 constituents	
	Ampl. (cm)	Phase (deg)	Ampl. (cm)	Phase (deg)	Ampl. (cm)	Phase (deg)
Nikiski	069/089	307/291	039/039	291/255	006/009	290/249
Seldovia	056/065	279/270	034/028	263/246	006/007	258/242
Anchorage	069/112	341/299	039/047	322/268	006/010	331/257

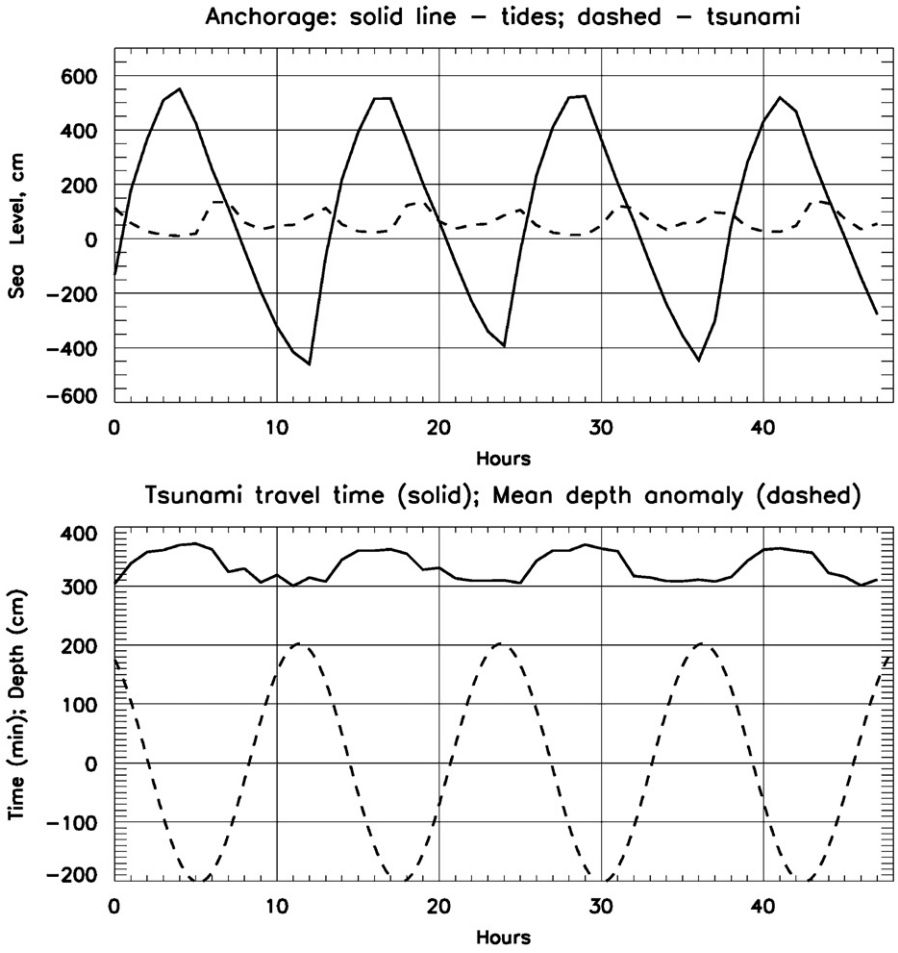

Fig. 7. Tsunami–tide interactions at Anchorage. Upper panel shows tide (solid line) and the magnitude of the maximum tsunami signal at Anchorage at different tidal phases (dashed line). The bottom panel shows time (minutes) of tsunami travel from the open boundary to Anchorage. The travel time changes depending on tidal phase when this tsunami is generated at the open boundary. The dashed line depicts the anomaly of mean Cook Inlet depth changes due to tides. The maximum travel time corresponds to the minimum mean Cook Inlet depth.

tidal elevations and tidal velocity amplitudes and phases for seven major waves. Fig. 6 shows some results for the major M2 and K1 constituents. The simulated tidal elevations (see Tables 2 and 3) are a bit larger than those observed (except for Anchorage), but the phases of tide propagation are in good agreement with observations.

In our next experiment, we simulated tides in CI for all 7 waves interacting together for a 3-month period (long-period tides were not taken into account, time was conditional starting from zero; tidal phases were relative to Greenwich meridian), and results for the last month's calculations (sea level time series with sampling interval of 1 h) were used to calculate tidal parameters for major tide gauge locations where tidal constituents are known from observations (Anchorage, Nikiski, Seldovia). The simulation of all tidal constituents improved the accuracy of simulated tidal parameters, and amplitudes of tides for all tidal constituents were somewhat, but not significantly, better than those shown in Tables 2 and 3. In general, the underestimation of tidal amplitude relative to observed tides was less than 12%. Based on these results, we assumed that tides were simulated well enough to start simulations of tsunami–tide interactions in CI.

The results of the tide-only model run after 2 months of simulations were saved and then used as initial conditions to continue simulations of tides and tsunamis together.

To model an abrupt bottom displacement, which generates tsunami we simulated 50 tsunami events by prescribing a positive half-cycle sinusoidal signal with an amplitude of 100 cm and a period of full cycle of 40 min at the southern boundary of the CI region (Fig. 5). The 40 min signal at this boundary (approximate depth 175 m) generates tsunami of approximately 100 km wavelength. At the eastern boundary, we used a combination of tidal elevations and radiation conditions for outgoing tsunami signals. The first tsunami was generated at a time corresponding to 1440 h after initiation of tidal calculations for 7 tidal constituents. After tsunami generation, these calculations were continued for the next 50 h, and tidal elevations and velocity data were collected at a set of grid points for analysis. The second tsunami was generated 1 h after initial tidal conditions were specified, and, again, calculations were continued for the next 50 h. The remaining 48 tsunami simulations were initiated at 1 h intervals and all started from the initial conditions described above. This allowed us to investigate how tsunami height changes, depending on time of tsunami generation at the open boundary and basically depending on tidal phase in the region.

Some results of these simulations are shown for Anchorage and Anchor Point in Figs. 7 and 8, respectively. The major indicator of tsunami–tide interactions is the tsunami's magnitude and its travel time to the region. In Anchorage, the tsunami is relatively small and adds from 5 to 135 cm to the total sea level elevation of tsunami–tide interactions at different tidal phases. This means that superposing two solutions where tides and tsunamis were calculated separately results in a maximum error of 135 cm or approximately 25% of tidal height, comparable to the tsunami height predicted for Anchorage (Fig. 7). Fig. 7 also shows that it is most likely that, for this point, the maximum tsunami signal can be expected between low and high tide when the tide is in transition from low to high in Anchorage; and a tsunami minimum is always observed at high tide and an intermediate minimum at low tide.

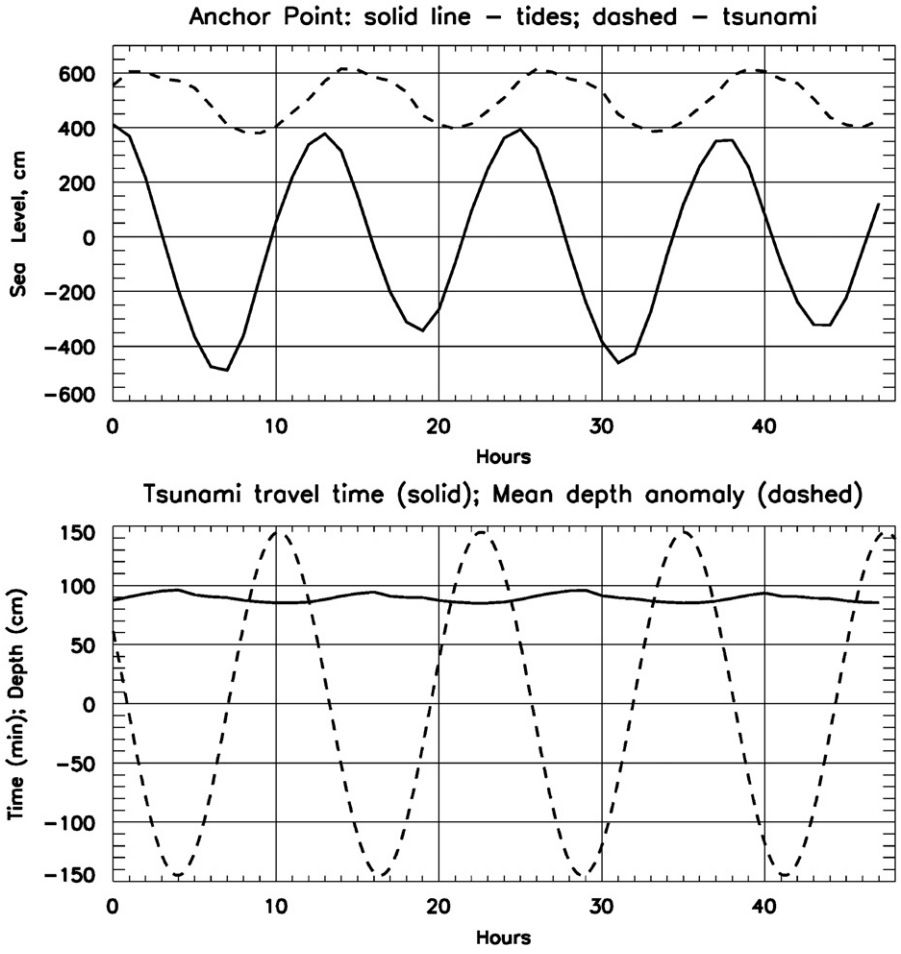

Fig. 8. Tsunami–tide interactions at Anchor Point. The upper panel shows tide (solid line) and the magnitude of the maximum tsunami signal at Anchor Point at different tidal phases (dashed line). The bottom panel shows travel time (minutes) of the tsunami signal from the open boundary to Anchor Point. The travel time changes depending on tidal phase when the tsunami is generated at the open boundary.

The tsunami arrival time at Anchorage also changes depending on tidal phase. This time is minimal when tide at Anchorage is low and maximal when tide at Anchorage is high. This does not contradict our previous section results where we concluded that the tsunami signal propagates faster at high tide and slower at low tide. The tidal signal takes approximately 5 h and 30 min (Fig. 7) to travel from the open boundary of Cook Inlet to Anchorage; during this interval, the tsunami interacts with the tide at different tidal phases and elevations in different regions, and, therefore, at Anchorage we observe an integrated result of tsunami–tide interaction. Tsunami travel time to Anchorage when tsunami signals are simulated with tides varies from 5 h to 6 h and depends on tidal phase (Fig. 7). There is a good correlation between tsunami travel time to Anchorage and an anomaly of total Cook Inlet depth, $D=H+\zeta$, which changes with tides (Fig. 7, bottom panel).

At Anchor Point, the potential tsunami adds from 395 to 605 cm to the total sea level elevation of tsunami–tide interactions at different tidal phases. This means that superposing two solutions, where tides and tsunamis were calculated separately, results in a maximum error of 210 cm or ~52% of tidal height and ~30% of potential tsunami height (Fig. 8). For Anchor Point, the maximum tsunami occurs approximately 70–90 min after high tide at this site, and the minimum tsunami magnitude is observed approximately 70–90 min after low tide (Fig. 8). The tsunami arrival time to Anchor Point varies between 85 and 96 min, depending on tidal phase, and it is minimal when the anomaly of the total Cook Inlet depth (between open boundary and Anchor Point) reaches maximum and maximal when the tsunami propagates at low tide/depth (Fig. 8).

Similar to our conclusions associated with tsunami–tide interactions in an idealized channel, we found that the major cause of tsunami height dependence on tides is related to changes in the total depth of the region when the tsunami rides the tide (Figs. 7 and 8, bottom panels).

5. Summary and discussion

We investigated some aspects of tsunami–tide interactions based on idealized and realistic numerical experiments. Theoretically, by changing total ocean depth, tidal elevations influence the speed and magnitude of tsunami waves in shallow regions with dominating tidal signals. We tested this assumption by employing a simple 1-D model that describes propagation of tidal waves in a channel with gradually increasing depth and the interaction of the tidal waves with tsunamis generated at the channel's open boundary. Results of this work show that tsunami–tide interactions can easily be detected in shallow regions. Important conclusions from our idealized studies are that computed elevations by simulating the tsunami and the tide together differ significantly from linear superposing of the sea surface heights obtained when simulating the tide and the tsunami separately, and that maximum tsunami–tide interaction depends on tidal amplitude and phase. The major cause of this tsunami–tide interaction is tidally induced ocean depth that changes the conditions of tsunami propagation, amplification, and dissipation. Interactions occur by means of momentum advection, bottom friction, and variable water flux due to changing total depth and velocity. There is interplay among these factors but, without including friction and inertial effects, we found the major cause of tsunami–tide interactions to be changing depth (expressed by fluxes in the equation of continuity).

These preliminary idealized experiments allowed us to analyze and understand important tsunami–tide interactions in Cook Inlet, Alaska. Cook Inlet has high tides and a history of strong tsunamis and is a potential candidate for tsunami impacts in the future. We simulated realistic tides and studied tsunami–tide interactions for two sites (Anchorage and Anchor Point) that have different coastline and bathymetry configurations and different ranges of tides and tsunamis. At Anchor Point, it would be expected that a potential tsunami would be amplified by a factor from 4 to 6 relative to the tsunami magnitude at the open boundary, depending on the tidal phase when this tsunami is introduced at the open boundary. At Anchorage, a potential tsunami can be damped (factor of 0.05) or lightly amplified (factor of 1.35) depending on the phase of the tide when this tsunami entered the Cook Inlet region via its open boundary. We also found that superposing two solutions where tides and tsunamis were calculated separately in order to predict the total tsunami impact results in a maximum error of 210 cm or ~52% of tidal height and ~30% of potential tsunami height at Anchor Point, while at Anchorage there is a maximum error of 135 cm or 20% of tidal height at Anchorage. For Anchor Point, the travel time from the open boundary to this site takes from 85 to 90 min, depending on tidal phase, and the error in the tsunami prediction can be as much as 5 min, while at Anchorage this error can be as much as 60 min.

The major conclusion from our idealized and regional studies is that tsunami–tide interactions have a very wide range of expression because these processes are very individual for different basin bathymetries, coastline configurations, and particular features of tsunami and tidal forcing. With this in mind, our general recommendation is to simulate tsunamis together with tides where tides are strong and where their magnitudes are comparable to prevailing depths. This approach can reduce uncertainties in tsunami predictions.

Existing numerical models presently employed by the tsunami warning centers do not presently include the tides or tsunami–tidal interactions but they can be substantially improved with no loss of speed by including the tides.

A simple step towards including tide–tsunami interactions is to use practical approach by Whitmore and Sokolowski, (1996) which they applied for tsunami calculation only by pre-computing all the required parameters. The approach results in running a slate of scenarios for every possible permutation and combination of epicenter locations, rupture parameters, and focal depths. When a tsunami occurs, these pre-computed scenarios can be used to determine the closest match, and this matching case can be used along with observed sea level fluctuations for tsunami warning guidance. This practical approach can be straightforwardly extended to include tsunami–tide interactions.

Acknowledgements

We thank two anonymous reviewers for comments that greatly improved the paper. This publication is the result in part of research sponsored by the Cooperative Institute for Arctic Research (CIFAR) with funds from the National Oceanic and Atmospheric Administration (NOAA) under cooperative agreement NA17RJ1224 with the University of Alaska.

References

Durran, D.R., 1999. In: Numerical Methods for Wave Equations in Geophysical Fluid Dynamics. Springer 465 pp.

Dixon, M.J., Tawn, J.A., 1997. Estimates of extreme sea conditions: spatial analyses for the UK coast. Proudman Oceanographic Laboratory Internal Document No. 112.

Egbert, C.D., Bennett, A.F., Foreman, M.G.G, 1994. Topex/Poseidon tides estimated using a global inverse model. J. Geophys. Res. 99, 24821–24852.

Ezer, T., Liu, H., 2009. Combining remote sensing data and inundation modeling to map tidal mudflat regions and improve flood predictions: a proof of concept

demonstration in Cook Inlet, Alaska. Geophys. Res. Lett. 36, L04605, doi:10.1029/2008GL036873.
Ezer, T., Hobbs, R., Oey, L.-Y., 2008. On the movement of beluga whales in Cook Inlet, Alaska: simulations of tidal and environmental impacts using a hydrodynamic inundation model. Oceanography 21 (No. 4), 186–195.
Flather, R.A., 1976. A tidal model of the north-west European continental shelf. Mem. Soc. R. Sci. Liege 6 (10), 141–164.
Houston, J.R., Garcia, A.W., 1978. Type 16 Flood Insurance Study: tsunami predictions for the west coast of the continental United States. USACE Waterways Experimental Station Technical Report H-78-26.
Johnson, M.A., Okkonen, S.R. (Eds.), 2000. Proceedings Cook Inlet Oceanography Workshop.November 1999, Kenai, AK. Final Report. OCS Study MMS 2000-043, University of Alaska Coastal Marine Institute, University of Alaska Fairbanks and USDOI, MMS, Alaska OCS Region, 118 pp.
Kowalik, Z., Knight, W., Logan, T., Whitmore, P., 2005. Numerical modeling of the global tsunami: Indonesian tsunami of 26 December 2004. Sci. Tsunami Hazards 23 (1), 40–56.
Kowalik, Z., Proshutinsky, T., Proshutinsky, A., 2006. Tide-tsunami interactions. Sci. Tsunami Hazards 24 (4), 242–256.
Lander, J.F., Lockridge, P.A., 1989. United States Tsunamis. National Geophysical Data Center, Boulder 265 pp.
Matthews, J.B., Mungall, J.C.H., 1972. A numerical tidal model and its application to Cook Inlet, Alaska. J. Mar. Res. 15, 27–38.
Mofjeld, H.O., Foreman, M.G.G., Ruffman, A., 1997. West coast tides during Cascadia subduction zone tsunamis. Geophys. Res. Lett. 24 (17), 2215–2218.
Mofjeld, H.O., González, F.I., Titov, V.V., Venturato, A.J., Newman, J.C., 2007. Effects of tides on maximum tsunami wave heights: probability distributions. J. Atmos. Oceanic Tech. 24 (1), 117–123.
Oey, L.-Y., Ezer, T., Hu, C., Muller-Karger, F., 2007. Baroclinic tidal flows and inundation processes in Cook Inlet, Alaska: numerical modeling and satellite observations. Ocean Dyn. 57, 205–221, doi:10.1007/s10236-007-0103-8.
Patchen, R.C., Bruce, J.T., Connolly, M.J., 1981. Cook Inlet circulatory survey: 1973-75. NOS Oceanographic Circulatory Survey Report No. 4, Rockville, Md., 89 pp.
Bernard, Eddie N., Robinson, Allan R. (Eds.), The Sea, vol. 15, Tsunamis. Harvard University Press, Cambridge, MA, 2009, 450 pp.
Weisz, R., Winter, C., 2005. Tsunami, tides and run-up: a numerical study. In: Papadopoulos, G.A., Satake, K. (Eds.), Proceedings of the International Tsunami Symposium, Chania, Greece, 27–29 June, 2005, 322 pp.
Whitmore, P.M., Sokolowski, T.J., 1996. Predicting tsunami amplitudes along the North American coast from tsunamis generated in the northwest Pacific Ocean during tsunami warnings. Sci. Tsunami Hazards 14, 147–166.